Progress In Electromagnetics Research, PIER 80, 161–178, 2008

AUTOMATIC INCORPORATION OF SURFACE WAVE POLES IN DISCRETE COMPLEX IMAGE METHOD

L. Zhuang

School of Electronic Information
Wuhan University
Wuhan 430079, China

W. Hu and W. Yu

ATR Lab.
National University of Defense Technology
Changsha 410073, Hunan, China

G.-Q. Zhu

School of Electronic Information
Wuhan University
Wuhan 430079, China

Y. H. Zhang

School of Electronic and Engineering
University of Leeds
UK

Abstract—Discrete complex image method is introduced to get a closed-form dyadic Green's function by a sum of spherical waves. However, the simulation result by the traditional discrete complex image method is only valid in near-field for several wavelengths. In this paper, we analyze the form of spectral domain dyadic Green's function in the whole k_ρ plane and the variety of valid range of simulation results by different sampling paths in two-level discrete complex image method. Consequently, for dyadic Green's function, surface wave pole contribution both in spectral domain and spatial domain is clarified. We introduce the automatic incorporation of surface wave poles in discrete complex image method without extracting surface wave poles. The contribution of surface wave poles in spectral domain and spatial domain dyadic Green's function is further confirmed in the new

method. Besides, this method can represent dyadic Green's function by spherical waves in the layer where the source and field points are. So it satisfies the splitting requirement and consequently reduces the computational complexity dramatically especially for objects with large scale in $\hat{z}$ direction.

1. INTRODUCTION

One of the most widely studied topics in applied electromagnetics is that of wave interaction with planarly layered media model. It can find various applications in geophysics exploring [1], unexploded objects characterizing, and microwave integrated circuit analyzing, etc. This structure can be efficiently and rigorously analyzed by the method of moments (MoM) [2–4] and fast algorithms based on MoM, such as the conjugate gradient fast Fourier transform method [5], the adaptive integral method [6], the fast multipole method [7]. Either for the conventional MoM or fast algorithms, dyadic Green's function for layered media should be computed. However, dyadic Green's function is expressed in an infinite integral with an oscillatory and slowly decaying kernel, and the evaluation of dyadic Green's function is quite time consuming.

The discrete complex image method [9–18, 28] is an efficient and widely used method for rapidly evaluating spatial domain Green's function [28]. Essentially, the basic idea of discrete complex image method is to convert the spectral domain dyadic Green's function to a closed form spatial domain dyadic Green's function by approximating method and Sommerfeld identity. The unparalleled advantage of discrete complex image method is that it can represent spatial dyadic Green's function in an analytical expression.

However, there exists limitation of traditional discrete complex image method, since the simulation result by discrete complex image method is only valid in near-field for several wavelengths. Usually, this limitation is attributed to the absence of surface wave modes in conventional discrete complex image method. In previous investigations [19], surface wave poles were specially extracted before applying discrete complex image method, and the surface wave contribution was incorporated by residuals theory. Unfortunately, the extraction of surface wave poles in spectral domain Green's function is quite a difficult task, and it brings up extra computational load. Meanwhile, another remedy, the two-level discrete complex image method [11] was proposed. The two-level discrete complex image method employed a dual-sampling-rate scheme to balance

approximation accuracy and complexity. It can yield larger valid range without extracting the quasi-static and surface wave contributions. But the valid range of two-level discrete complex image method is still relative small for electrically large problems.

Recently, Yuan [17] proposed an improved method to make the simulation results accurate in medium- and far-field, by deforming the sampling path in discrete complex image method. But it can only represent dyadic Green's function by spherical waves in free space. Consequently, the vertical coordinate z and z' can not be extracted and numerous discrete complex image method approximations are required, especially for objects with large scale in $\hat{z}$ direction [20]. In this paper, we contrive a novel deformed sampling path for discrete complex image method, which not only can get accurate simulation results in medium- and far-field but also ensures the extraction of z and z'.

Moreover, and most importantly, we make clear the contribution of surface wave in spectral domain dyadic Green's function. Based on this finding, we can contrive any sampling path that runs closely by the singular points. In this way, the fast variations around surface wave poles can be sampled in approximating functions. Consequently, the surface wave poles contribution can be automatically incorporated in spatial domain dyadic Green's function with closed form. The clarification of surface wave poles character in spectral domain dyadic Green's function provides rules for choosing sampling path of discrete complex image method.

The procedure of the two-level discrete complex image method is described and discussions associated with this approach are demonstrated on some examples by using the this method in Section 2. And a new sampling path which can automatically incorporate the contribution of surface wave poles is shown in Section 3. Then some numerical examples are included in Section 4. Finally, Section 5 provides conclusion.

2. TWO-LEVEL DISCRETE COMPLEX IMAGE METHOD AND DISCUSSIONS

For the sake of illustration, consider a general planarly layered media as shown in Fig. 1, where the source is a horizontal electric dipole (HED). N parallel layers have different heights, permittivities, conductivities and permeabilities, which are represented as d_i, ε_i, σ_i and $\mu_i\,(i = 1, 2 \ldots N)$, respectively. And effective permittivity is defined as $\tilde{\varepsilon} = \varepsilon'\,(1 - j\tan\delta)$. In this paper, we focus on the situation when the source and field points are in the same layer.

Dyadic Green's function describes the relationship between

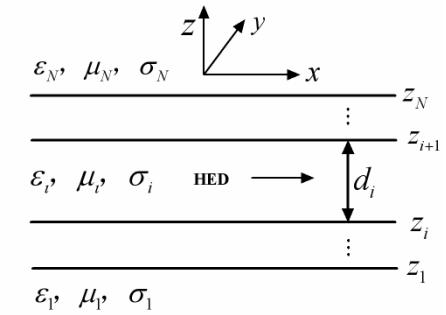

Figure 1. Typical layered media with a HED in layer i.

current source and electric field in given media background. Suppose only electric currents are present, electric field generated by current source and boundary can be formulated in the mixed-potential integral equation (MPIE) as follows [23]:

$$E = -j\omega\mu_0 \left\langle \bar{G}^A; J \right\rangle + \frac{1}{j\omega\varepsilon_0} \nabla \left(\left\langle K^\Phi; \nabla' \cdot J \right\rangle + \left\langle C^\Phi \hat{z}; J \right\rangle \right) \quad (1)$$

where J and E are electric source and field respectively. Moreover, $\bar{G}^A$ is the vector potential dyadic Green's function. K^Φ is the scalar potential kernel and C^Φ is the correction factor associated with the longitudinal electric currents. The notation $\langle\ ;\ \rangle$ denotes integrals of products of two functions separated by the comma over the source region where J exists.

To get the induced current J, dyadic Green's function should be evaluated beforehand. A simple and effective way to get a dyadic Green's function for planarly layered media is the spectral domain transmission line method [23], in which each layer is dealt with as a component in a transmission line. The spatial domain Green's functions may be obtained by employing a one-dimensional Hankel transformation of the corresponding spectral domain Green's functions as

$$\bar{G}(r) = \frac{1}{4\pi} \int_{\text{SIP}} dk_\rho k_\rho^{n+1} H_n^{(2)}(k_\rho\rho) \tilde{\bar{G}}(k_\rho), \quad n = 0, 1 \quad (2)$$

where SIP stands for Sommerfeld integral path, $H_n^{(2)}(k_\rho\rho)$ is the nth-order Hankel function of the second type, and $\bar{G}(r)$ and $\tilde{\bar{G}}(k_\rho)$ are the spatial domain and spectral domain dyadic Green's function, respectively.

Since the integrant of Sommerfeld integral in (2) is oscillatory and slowly decaying, it is time-consuming to evaluate spatial dyadic Green's

function by numerical integration. Discrete complex image method is a prominent and widely used method for rapidly evaluating of spatial domain dyadic Green's function.

In order to illustrate the limitation of conventional two-level discrete complex image method and its improvement proposed in this paper, a sample of spectral domain dyadic Green's function is given. We consider $\tilde{G}^{xx}_{Aii}$ of a horizontal electric dipole (HED) [10].

$$\begin{aligned}\tilde{G}^{xx}_{Aii} &= \frac{\mu_i}{2jk_{zi}}\Big\{e^{-jk_{zi}|z-z'|} + \tilde{R}^{TE}_{i,i+1}M^{TE}_i \\ &\quad \times \left[e^{jk_{zi}(z+z'-2z_{i+1})} + \tilde{R}^{TE}_{i,i-1}e^{jk_{zi}(z-z'-2d_i)}\right] \\ &\quad +\tilde{R}^{TE}_{i,i-1}M^{TE}_i\left[e^{-jk_{zi}(z+z'-2z_i)} - \tilde{R}^{TE}_{i,i+1}e^{-jk_{zi}(z-z'+2d_i)}\right]\Big\} \quad (3)\end{aligned}$$

where general reflection coefficients $\tilde{R}^{TE}_{i,i-1}$, $\tilde{R}^{TM}_{i,i+1}$ and M^{TE}_i are defined in [10].

For the configuration given in Fig. 1, there are two branch-point singularities in spectral domain dyadic Green's function. The branch points are related with the outermost semi-infinite half space. Besides, there are surface wave pole singularities between the minimum and the maximum wavenumbers of the layers. Furthermore, the spectral domain dyadic Green's function is even function of k_ρ, so the poles always come in pairs. For lossless dielectrics, singular poles lie on the real k_ρ axis. For lossy dielectrics, they migrate into the fourth quadrants of the k_ρ plane. The number of surface wave poles is dependent on the electrical thicknesses and the dielectric constants of layers involved [14].

The basic idea of discrete complex image method is to approximate dyadic Green's function with a sum of spherical wave functions with closed form. In discrete complex image method, the spectral domain dyadic Green's function is firstly expressed as a sum of complex exponential series via Prony approximation [21] or the generalized pencil-of-function approximation method [22].

$$\tilde{G}(k_\rho) \cong \frac{1}{2jk_{zi}}\sum_{m=1}^{N} a_m e^{-b_m k_{zi}} \quad (4)$$

Then the spatial domain dyadic Green's function $\tilde{G}^{xx}_{Aii}$ can be represented as a sum of spherical waves by applying the Sommerfeld identity as shown in (5).

$$\frac{e^{-jkr}}{r} = \int_{SIP} dk_\rho k_\rho H^2_0(k_\rho\rho)\frac{e^{-jk_z|z|}}{2jk_z} \quad (5)$$

For Green's functions that have $\cos\phi$ or $\sin\phi$ dependency can be represented as a sum of spherical waves by applying the derivative of the Sommerfeld identity (5), which is

$$(1+jkr)\frac{\rho e^{-jkr}}{r^3} = \int\limits_{SIP} dk_\rho k_\rho^2 H_1^2(k_\rho\rho)\frac{e^{-jk_z|z|}}{2jk_z} \tag{6}$$

Before applying discrete complex image method, the surface wave poles should be extracted to get wider valid range of simulation results. Later a two-level discrete complex image method without the extraction of surface wave poles was proposed to reduce the approximation complexity and to extend the valid range. In the two-level discrete complex image method [11], a dual sampling-rate scheme is adopted and the sampling path is deformed as follows:

$$C_{ap1} : k_{zi} = -jk_i[T_{cut2} + t] \qquad 0 \le t \le T_{cut1}, \tag{7}$$

$$C_{ap2} : k_{zi} = k_i\left[-jt + \left(1 - \frac{t}{T_{cut2}}\right)\right] \qquad 0 \le t \le T_{cut2} \tag{8}$$

Where C_{ap1} and C_{ap2} denote the two sampling path, k_i and k_{zi} are the wavenumber and the vertical wavenumber for the ith layer respectively. T_{cut1} and T_{cut2} are the constants controlling the form of deformed path.

Samples of spectral domain dyadic Green's functions are evaluated along the sampling path and then the sampled spectral domain dyadic Green's function can be approximated by complex exponentials. At last, the spatial domain dyadic Green's function can be represented in series of spherical waves via Sommerfeld identity in (5).

$$G(r,r') = \frac{1}{4\pi}\left[\sum_n^{N_1} a_{1n}\frac{e^{-jk_i r_{1n}}}{r_{1n}} + \sum_n^{N_2} a_{2n}\frac{e^{-jk_i r_{2n}}}{r_{2n}}\right] \tag{9}$$

Usually, the simulation results of two-level discrete complex image method are accurate for the distance as far as $3 \sim 4$ wavelengths and they fall into errors beyond this range. But what is the cause of the inaccuracy and how to extend the valid range? It is instructive to investigate the relationship between sampling path and valid range of simulation results. In other words, it is important to make clear which factors affect the valid range and how they are incorporated.

To answer the aforementioned questions, a five-layer geometry with infinite conducting base is considered, as shown in Fig. 2. The structure and electromagnetic parameters are given in Fig. 2, and the frequency is 30 GHz.

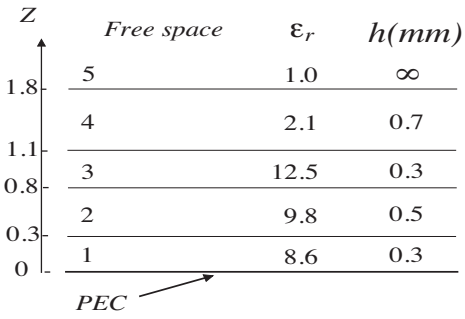

Figure 2. Geometry of a structure with five layers and a perfectly conducting ground plane.

We consider G_{A22}^{xx} of dyadic Green's function, in which both source point and field point reside at 0.4 mm, in the second layer. In utilizing two-level discrete complex image method, T_{cut1} and T_{cut2} should be chosen according to the layer parameters. For comparison, we first fix $T_{cut1} = 200$, and then appoint different values for T_{cut2} to form different sampling path C_{ap2} for different approximations. Here, we choose $T_{cut2} = 2$, 5, 8, respectively.

Figure 3 shows the value distribution of $\tilde{G}_{A22}^{xx}(k_\rho, z, z')$ in k_ρ plane. It indicates large variations due to the singular point. Fig. 4 depicts different sampling paths for different value of T_{cut2}. The singular points

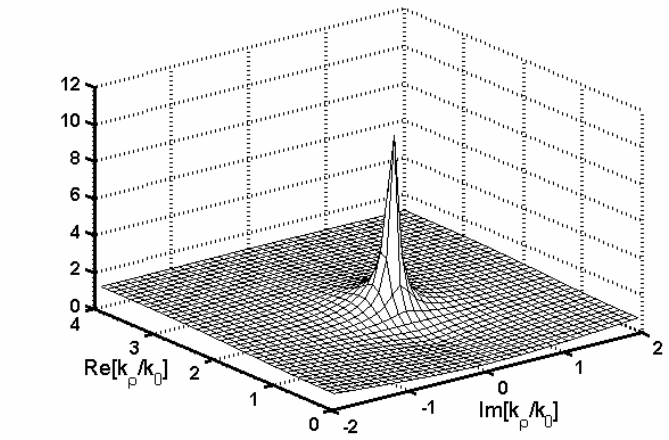

Figure 3. The value distribution of spectral domain $\tilde{G}_{A22}^{xx}(k_\rho, z, z')$ in k_ρ plane.

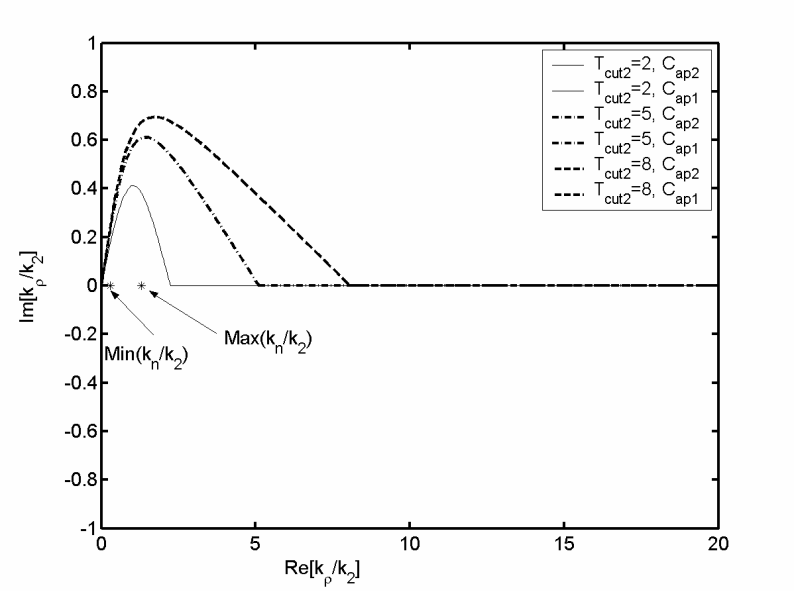

Figure 4. Comparison of different sampling paths for T_{cut2}.

locate at the real axis of k_ρ plane, and the sampling paths travel along the real k_ρ axis as the Sommerfeld integral path does. However, the most importantly, sampling paths shown in Fig. 4 try to avoid coming close to the singular points, and the larger is T_{cut2}, the farther is the sampling path from the singular points. Fig. 5 shows simulation results for different sampling paths according to T_{cut2}. For smaller value of T_{cut2}, the simulation result has larger valid range. As shown in Fig. 5, sampling scheme for $T_{cut2} = 2$ yields the largest valid range.

Based on the analysis of Fig. 3, Fig. 4 and Fig. 5, we can conclude that if the sampling path is closer to singular points, the valid range is larger. Since the singular points in spectral domain contribute as surface wave modes in spatial domain, and the surface wave dominates in far region of spatial domain dyadic Green's function. In this way, we can go further to conclude that the sampling path which is moved closer to singular points can catch the more variations of the singular points, and consequently can approximate the surface wave modes efficiently.

It is instructive to make clear that the contribution of surface wave poles can be incorporated in simulation result by choosing a sampling path which is close to singular points.

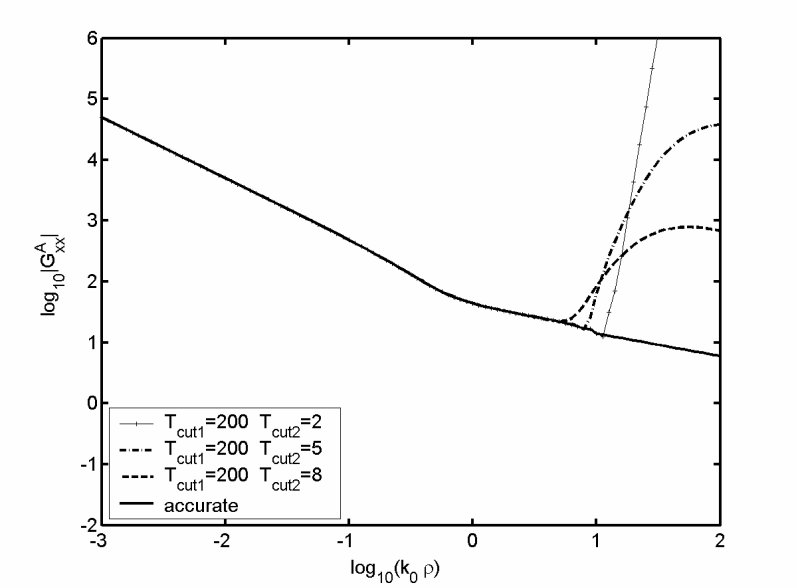

Figure 5. Comparison of results of G_{A22}^{xx} for different T_{cut2}.

3. THE NEW SAMPLING PATH

It is found that if the sampling path is closer to singular points, the more variations of spectral domain dyadic Green's function can be extracted. Consequently the larger valid range can be obtained in spatial domain dyadic Green's function. Guided by this new finding, we contrive to design a new sampling path to get large valid range for discrete complex image method.

The key of extending valid range lies in incorporating the contribution of singular points. As we have mentioned beforehand, there are some singular points in the geometry, that is, in the range of $k_{\min}\,(=k_0) < k_\rho < k_{\max}\,(=k_0\sqrt{\tilde{\varepsilon}_{\max}})$ at the real k_ρ axis for lossless dielectrics. So the singulary points on the real axis of k_{zi} plane are between $[0, k_0\sqrt{\tilde{\varepsilon}_i - 1})$, and on the imaginary axis are between $(-jk_0\sqrt{\tilde{\varepsilon}_{\max} - \tilde{\varepsilon}_i}, 0]$. Moreover, there is no conceptual difficulty in using the same equations for treating the lossy substrate case. The path is the same in the k_{zi} plane. But the path in k_ρ plane may be a little difficult when $\alpha\beta < \varepsilon_i' \tan\delta/2$. As in that case, the point k_s moves in the four quadrant of k_ρ plane.

To extract the fast variations of singular points, we propose a deformed sampling path which passes across singular points in vicinity

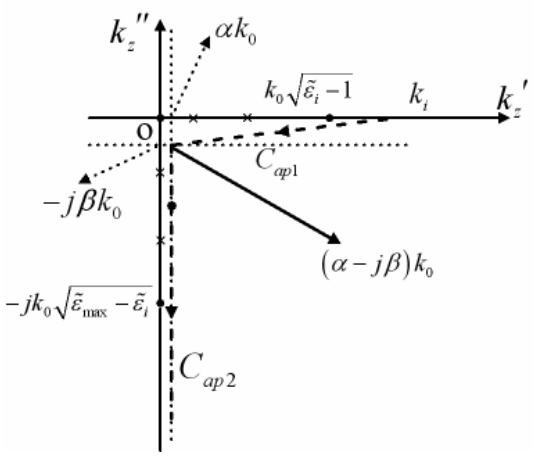

Figure 6. The new deformed sampling path in k_{zi} domain.

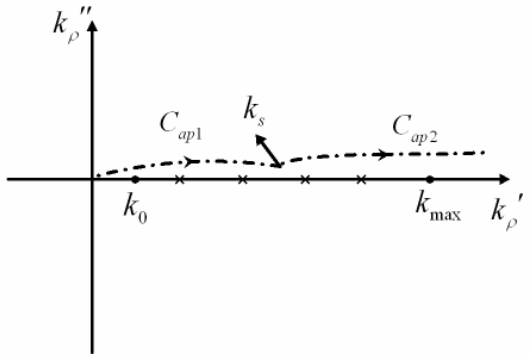

Figure 7. The new deformed sampling path in k_ρ domain.

as shown in Fig. 6.

$$C_{ap1} : k_{zi} = k_i(1 + (s-1)t), \qquad 0 \le t \le 1 \tag{10}$$

$$C_{ap2} : k_{zi} = k_i\left(s - j\frac{t}{\sqrt{\tilde{\varepsilon}_i}}\right), \qquad 0 \le t \le T \tag{11}$$

where $s = (\alpha - j\beta)/\sqrt{\tilde{\varepsilon}_i}$, $(0 < \alpha < 1,\ 0 \le \beta < 1)$ is the inflexion of sampling path.

In Fig. 6, α controls the distance between path C_{ap2} and imaginary axis of k_{zi} plane, and β controls the distance between path C_{ap1} and real axis of k_{zi} plane.

Because the path of integration is the legitimately deformed path from Sommerfeld integral path and over which the integrands are single-valued functions, the deformed path will not cross the branch point [14]. If the source and field points are in the free space layer, the new sampling path will be equal to the direct discrete complex image method by choosing $\beta = 0$.

The recipe of the new sampling path is as follows.

1) Approximate the spectral kernel on path C_{ap2} as

$$\tilde{G}\left(k_\rho\right)\Big|_{C_{ap2}} \approx \sum_{i=1}^{M} a_i e^{-jb_i k_{zi}}\Bigg|_{C_{ap2}} \tag{12}$$

To include enough information of all singular points on or near the imaginary axis, T should satisfy $T > \sqrt{\tilde{\varepsilon}_{\max} - \tilde{\varepsilon}_i}$. M can be over 100 for accurate requirements for the spatial-domain Green's function. The sampling path is closer to the singular points for smaller α.

2) Approximate the spectral kernel on path C_{ap1} as

$$\tilde{G}\left(k_\rho\right)\Big|_{C_{ap1}} - \sum_{i=1}^{M} a_i e^{-jb_i k_{zi}}\Bigg|_{C_{ap2}} \approx \sum_{i=1}^{N} a'_i e^{-jb'_i k_{zi}}\Bigg|_{C_{ap1}} \tag{13}$$

To include enough information of all singular points on or near the real axis, N can be over 100 for accurate requirements for the spatial-domain Green's function. The sampling path is closer to the singular points for smaller β.

3) The spatial-domain GF can be expressed as

$$G\left(\rho, z \middle| z'\right) = \sum_{i=1}^{M} a_i \frac{e^{-jk_i r_i}}{r_i} + \sum_{i=1}^{N} a'_i \frac{e^{-jk_i r'_i}}{r'_i} \tag{14}$$

where

$$r_i = \sqrt{\rho^2 + (z + z' - jb_i)^2} \tag{15}$$

A threshold *tol* can be set in the matrix pencil method [23] to control the accuracy. We set $tol = 10^{-8}$ both on C_{ap1} and C_{ap2}.

The improved path of k_{zi} domain can represent dyadic Green's function by spherical waves in the layer where the source and field points are, and it exactly satisfies the requirement of splitting scheme [20]. In that case, the vertical coordinate z and z' can be extracted and only a few coefficients $\tilde{R}^{TE}_{i,i\pm1} M^{TE}_i$ and $\tilde{R}^{TE}_{i,i-1} \tilde{R}^{TE}_{i,i+1} M^{TE}_i$

need to be handled by discrete complex image method. Thus the novel deformed path reduces the computational complexity dramatically especially with large scale in the vertical direction $\hat{z}$.

Although the similar idea has been proposed by the direct discrete complex image method [17], it can only represent dyadic Green's function by spherical waves in free space, so it doesn't meet the splitting requirement if the source and field points are not in the free-space layer. The vertical coordinate z and z' can't be extracted and numerous discrete complex image method approximations are required, especially for objects with large scale in $\hat{z}$ direction. Besides, the direct discrete complex image method doesn't give the pole distribution analysis.

4. NUMERICAL RESULTS

4.1. Lossless Case

To demonstrate the influence of α and β on the spatial-domain dyadic Green's function, we use the microstrip problem as used in [25, Fig. 2]. $z = z' = 0$, and the frequency is 4.075 GHz. The first layer is the dielectric layer, and the second layer is the air region. The new path represents dyadic Green's function by spherical waves in the first layer.

The value of α, β ($s = (\alpha - j\beta)/\sqrt{\varepsilon_i}$), the number M of singular values, how far along the horizontal direction $\rho_{\max}$ can be reached accurately for the spatial-domain Green's function, and the CPU times in a Intel(R) Xeon (TM) MP 3.16 GHz are listed in Table 1. λ_0 in Table 1 is the wave length in the free space. The first line is the situation of the direct discrete complex image method in [17] (in this example, $\gamma = 0.2$, $T_0 = 8.39$). The other lines are the results of the new sampling path on the C_{ap1} and C_{ap2} in k_{z1} plane. The horizontal direction $\rho_{\max}$ in C_{ap2} is almost same with the change of α. It indicates that possible surface wave poles are on the real axis of k_{z1} plane. Note that although the computational load of the new sampling path is approximately equal to $O\left[(1/s)^3\right]$, the CPU time used for the computation of the Green's function is still negligible compared with the matrix solving part in the MoM [17].

We consider the same structure in [25, Fig. 2]. Fig. 8 shows the plots of G_q for two values of α_s and β_s together with the accurate results. They are both accurate with small ρ and go further along ρ.

In another example, the example is shown with the same structure in Fig. 2. We make the new sampling path represent dyadic Green's function by spherical waves in the second layer where the source and field points are. The results are shown in Fig. 9 with different values of α and β by the new sampling path and $\gamma = 0.2$. γ is the same

Table 1. performances of the new sampling path for the different αs and β_s.

α, β	M on C_{ap1}	M on C_{ap2}	$\rho_{\max}$	CPU-time(sec)
[17]	5	26	$15.92\lambda_0$	0.19
$\alpha = 0.2, \quad \beta = 0.2$	43	8	$44.86\lambda_0$	0.61
$\alpha = 0.2, \quad \beta = 0.1$	79	9	$79.77\lambda_0$	2.11
$\alpha = 0.2, \quad \beta = 0.05$	149	9	$159.15\lambda_0$	12.06

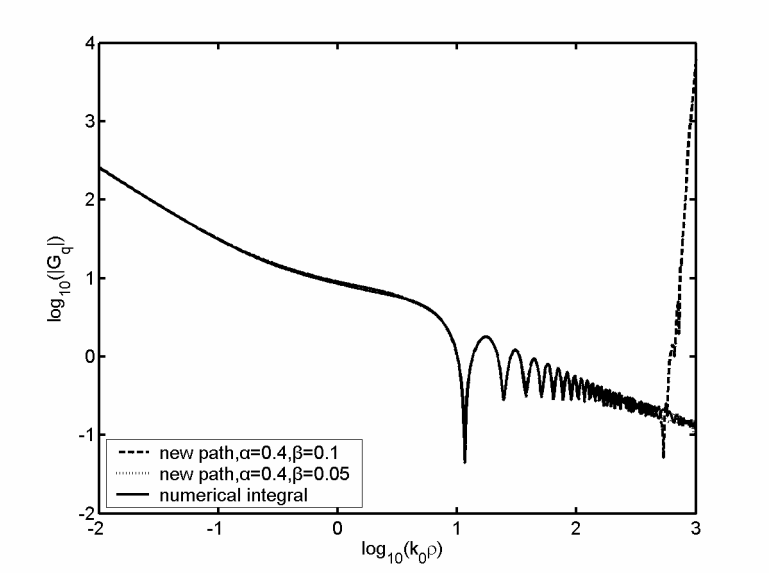

Figure 8. Spatial domain G_q obtained by new sampling path.

parameter used in [17]. It shows that the valid range is larger for smaller β. So it indicates the singular points are on the real axis of k_{z2} plane. The improvement of changing path from in k_{z5} plane [17] to in k_{z2} plane ensures the extraction of z and z'. Therefore, for large volume objects, especially that with large scale in the vertical direction $\hat{z}$, the splitting procedure cuts the time requirement dramatically [20].

4.2. Lossy Case

To show the efficiency of the new sampling path to calculate the dyadic Green's function in lossy structure, we consider the same lossy

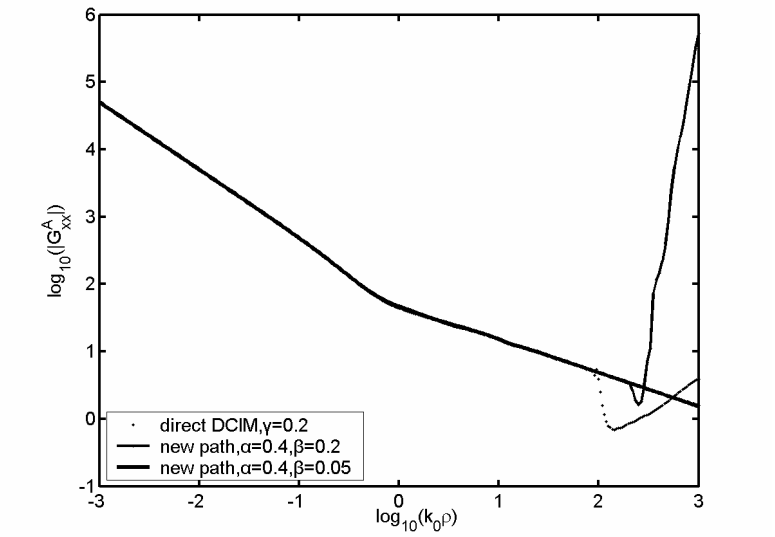

Figure 9. Spatial domain G_{A22}^{xx} obtained by new sampling path with different β.

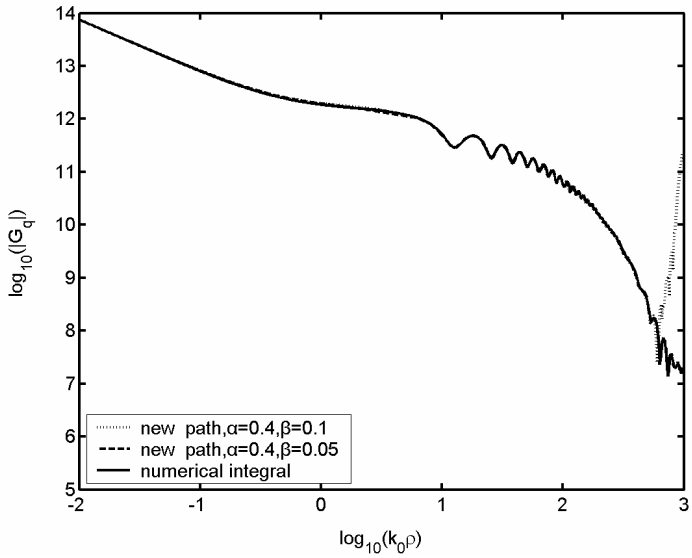

Figure 10. Spatial domain G_q obtained by the sampling path.

structure in [19]. For lossy cases, α, β don't need to satisfy the condition of $\alpha\beta \geq \varepsilon_i' \tan\delta/2$ [27]. Fig. 10 shows the plots of G_q for two values of α and β together with the numerical integral results. The path for $\alpha = 0.4$, $\beta = 0.05$ can approximate more accurate results in far field region than the path for $\alpha = 0.4$, $\beta = 0.1$, because some part of the former path is in the fourth quadrant of k_ρ plane where the surface wave poles are. And it indicates that the range for lossy cases still can be even accurate up to $160\lambda_0$ as for the lossless cases for small α, β.

5. CONCLUSION

In this paper we make clear the contribution of surface wave in spectral domain and spatial domain dyadic Green's function. Based on this finding, we contrive a new sampling path which can sample the fast variations around surface wave poles both for lossless and lossy media. And the range can even accurate up to $160\lambda_0$ both for both of them. So the surface wave poles contribution can be automatically incorporated in spatial domain dyadic Green's function with closed form. Besides, this new sampling path which can approximate the spatial domain Green's function by the wave number k_{zi} (i is the layer number where the source and field points are) ensures the extraction of z and z'. Therefore the method cuts the time requirement dramatically especially for objects with large scale in $\hat{z}$ direction.

ACKNOWLEDGMENT

The authors would thank the reviewers for their valuable comments and suggestions. And this work was supported in part by the National Natural Science Foundation of China under Grant no. 60671040.

REFERENCES

1. Van den Bosch, I., S. Lambot, M. Acheroy, I. Huynen, and P. Druyts, "Accurate and efficient modeling of monostatic GPR signal of dielectric targets buried in stratified media," *Journal of Electromagnetic Waves and Applications*, Vol. 20, 283–290, 2006.
2. Harrington, R. F., *Field Computation by Moment Methods*, Macmillan, New York, 1968.
3. Michalski, K. A. and D. Zheng, "Electromagnetic scattering and radiation by surface of arbitrary shape in layered media — Part I:

Theory," *IEEE Trans. Antennas Propag.*, Vol. 38, No. 3, 335–344, Mar. 1990.

4. Michalski, K. A. and D. Zheng, "Electromagnetic scattering and radiation by surface of arbitrary shape in layered media — Part II: Implementation and results for contiguous half-space," *IEEE Trans. Antennas Propag.*, Vol. 38, No. 3, 344–352, Mar. 1990.
5. Sarkar, T. K., E. Arvas, and S. M. Rao, "Application of FFT and the conjugate gradient method for the solution of electromagnetic radiation from electrically large and small conducting bodies," *IEEE. Trans. Antennas Propag.*, Vol. AP-34, No. 5, 635–640, May 1986.
6. Bleszynski, E., M. Bleszynski, and T. Jaroszewicz, "AIM: Adaptive integral method for solving large-scale electromagnetic scattering and radiation problems," *Radio Sci.*, Vol. 31, No. 5, 1225–1251, 1996.
7. Song, J., C. Lu, and W. C. Chew, "Multilevel fast multipole algorithm for electromagnetic scattering by large complex objects," *IEEE Trans. Antennas Propag.*, Vol. 45, No. 10, 1488–1493, Oct. 1997.
8. Saltykov, E. G., "The spectral expansion on the entire real line of Greens function for a three-layer medium in the fundamental functions of a nonself-adjoint sturm-liouville operator," *Progress In Electromagnetics Research Symposium, PIERS Online*, Vol. 2, No. 4, 344–346, 2006.
9. Aksun, M. I. and T. Onal, "Critical study of DCIM, and development of efficient simulation tool for 3D printed structures in multilayer media," *Progress In Electromagnetics Research Symposium, PIERS Online*, Vol. 2, No. 1, 35–37, 2006.
10. Dural, G. and M. I. Aksun, "Closed-form Green's function for general sources and stratified media," *IEEE Trans. Microw. Theory Tech.*, Vol. 43, No. 7, 1545–1552, Jul. 1995.
11. Aksun, M. I., "A robust approach for the derivation of closed-form Green's functions," *IEEE Trans. Microw. Theory Tech.*, Vol. 44, No. 5, 651–658, May 1996.
12. Jiang, L. J., W. C. Chew, and Y. C. Pan, "Capacitance extraction in the multilayer medium using DCIM and SMFMA," *Journal of Electromagnetic Waves and Applications*, Vol. 19, 1851–1864, 2005.
13. Liu, Y., L. W. Li, and M. S. Leong, "Calculation of spatial-domain green functions for multi-layered media using DCIM with automatic handling of surface wave poles," *Proc. Inst. Electr. Eng. — Microw. Antennas Prop.*, Vol. 151, No. 3, 236–240, 2004.

14. Aksun, M. I. and G. Dural, "Clarification of issues on the closed-form Green's functions in the stratified media," *IEEE Trans. Antennas. Propag.*, Vol. 53, No. 11, 3644–3653, Nov. 2005.
15. Kipp, R. A. and C. H. Chan, "Complex image method for sources in bounded regions of multilayer structures," *IEEE Trans. Microw. Theory Tech.*, Vol. 42, No. 5, May 1994.
16. Xu, X. B. and Y. F. Huang, "An efficient analysis of vertical dipole antennas above a lossy half-space," *Progress In Electromagnetics Research*, PIER 74, 353–377, 2007.
17. Yuan, M. T., T. L. Sarkar, and Salazar-Palma, "A discrete complex image method from the closed-form Green's functions in multilayered media," *IEEE Trans. Microw. Theory Tech.*, Vol. 54, No. 3, 1025–1032, Mar. 2006.
18. Soliman, E. A. and G. A. E. Vandenbosch, "Green's functions of filament sources embedded in stratified dielectric media," *Progress In Electromagnetics Research*, PIER 62, 21–40, 2006.
19. Polimeridis, A. G., T. V. Yioultsis, and T. D. Tsiboukis, "An efficient pole extraction technique for the computation of Green's functions in stratified media using a sine transformation," *IEEE Trans. Antennas Propag.*, Vol. 55, No. 1, 227–229, Jan. 2007.
20. Zhang, Y. H., B. X. Xiao, and G. Q. Zhu, "An improved weak-form BCGS-FFT combined with DCIM for analyzing electromagnetic scattering by 3-D objects in planarly layered media," *IEEE Trans. Geosci. Remote Sens.*, Vol. 44, No. 12, 3540–3546, Dec. 2006.
21. Van Blaricum, M. L. and R. Mittra, "Problem and solutions associated with Prony's method for processing transient data," *IEEE Trans. Antennas Propag.*, Vol. AP-26, No. 1, 174–182, Jan. 1978.
22. Hua, Y. and T. K. Sarkar, "Generalized pencil-of-function method for extracting poles for an EM system from its transient response," *IEEE Trans. Antennas Propag.*, Vol. 37, No. 2, 229–234, Feb. 1989.
23. Michalski, K. A. and J. R. Mosig, "Multilayered media Green's functions in integral equation formulations," *IEEE Trans. Antennas Propag.*, Vol. 45, No. 3, 508–519, Mar. 1997.
24. Sarkar, T. K. and O. Pereira, "Using the matrix pencil method to estimate the parameters of a sum of complex exponentials," *IEEE Antennas Propag. Mag.*, Vol. 37, 48–55, Feb. 1995.
25. Boix, R. R., F. Mesa, and F. Medina, "Application of total least squares to the derivation of closed-form Green's functions

for planar layered media," *IEEE Trans. Microw. Theory Tech.*, Vol. 55, No. 2, 268–280, Feb. 2007.

26. Boix, R. R., F. L. Mesa, and F. Medina, "Closed-form expressions for layered media Green's functions that are reliable both in the near field and in the far field," *Progress In Electromagnetics Research Symposium, PIERS Online*, Vol. 2, No. 6, 573–575, 2006.
27. Zhuang, L., G. Zhu, Y. Zhang, and B. Xiao, "An improved discrete complex image method for Green's functions in multilayered media," *Microw. Opt. Technol. Lett.*, Vol. 49, No. 6, 1337–1340, Jun. 2007.
28. Li, L. and Y. Xie, "Efficient algorithm for analyzing microstrip antennas using fast-multipole algorithm combined with fixed real-image simulated method," *Journal of Electromagnetic Waves and Applications*, Vol. 20, 2177–2188, 2006.
29. Slab, E. C., "Green's functions retrieval by crossconvolutions," *Progress In Electromagnetics Research Symposium, PIERS Online*, Vol. 3, No. 5, 736–740, 2007.